ADVANCED MATERIALS
www.advmat.de

Chemical Vapor Deposition of High-Optical-Quality Large-Area Monolayer Janus Transition Metal Dichalcogenides

Ziyang Gan, Ioannis Paradisanos, Ana Estrada-Real, Julian Picker, Emad Najafidehaghani, Francis Davies, Christof Neumann, Cedric Robert, Peter Wiecha, Kenji Watanabe, Takashi Taniguchi, Xavier Marie, Johannes Biskupek, Manuel Mundszinger, Robert Leiter, Ute Kaiser, Arkady V. Krasheninnikov, Bernhard Urbaszek, Antony George,* and Andrey Turchanin**

One-pot chemical vapor deposition (CVD) growth of large-area Janus SeMoS monolayers is reported, with the asymmetric top (Se) and bottom (S) chalcogen atomic planes with respect to the central transition metal (Mo) atoms. The formation of these 2D semiconductor monolayers takes place upon the thermodynamic-equilibrium-driven exchange of the bottom Se atoms of the initially grown $MoSe_2$ single crystals on gold foils with S atoms. The growth process is characterized by complementary experimental techniques including Raman and X-ray photoelectron spectroscopy, transmission electron microscopy, and the growth mechanisms are rationalized by first principle calculations. The remarkably high optical quality of the synthesized Janus monolayers is demonstrated by optical and magneto-optical measurements which reveal the strong exciton–phonon coupling and enable an exciton *g*-factor of −3.3.

1. Introduction

The physical properties of monolayer (ML) transition metal dichalcogenides (TMD) can be tailored for specific applications by stacking them in heterostructures,[1,2] alloying,[3] or more recently by preparing ML Janus TMDs.[4–6] Due to the difference in electronegativity of the top and bottom chalcogen layers, Janus TMDs possess an in-built electric dipole that breaks the out-of-plane plane mirror symmetry, leading to a manifold of novel physical phenomena such as, for example, strong Rashba splitting,[7] piezoelectric,[8] pyroelectric,[9] novel excitonic,[10] and valleytronic phenomena.[11]

Z. Gan, J. Picker, E. Najafidehaghani, C. Neumann, A. George, A. Turchanin
Institute of Physical Chemistry
Friedrich Schiller University Jena
07743 Jena, Germany
E-mail: antony.george@uni-jena.de; andrey.turchanin@uni-jena.de

I. Paradisanos, A. Estrada-Real, C. Robert, X. Marie, B. Urbaszek
Université de Toulouse
INSA-CNRS-UPS
LPCNO
Toulouse 31077, France

F. Davies, A. V. Krasheninnikov
Institute of Ion Beam Physics and Materials Research
Helmholtz-Centre Dresden-Rossendorf
01328 Dresden, Germany

P. Wiecha
LAAS-CNRS
Université de Toulouse
Toulouse 31400, France

The ORCID identification number(s) for the author(s) of this article can be found under https://doi.org/10.1002/adma.202205226.

DOI: 10.1002/adma.202205226

K. Watanabe
Research Center for Functional Materials
National Institute for Materials Science
Tsukuba 305-0044, Japan

T. Taniguchi
International Center for Materials Nanoarchitectonics
National Institute for Materials Science
Tsukuba 305-0044, Japan

J. Biskupek, M. Mundszinger, R. Leiter, U. Kaiser
Central Facility of Electron Microscopy
Electron Microscopy Group of Material Science
University of Ulm
D-89081 Ulm, Germany

A. V. Krasheninnikov
Department of Applied Physics
Aalto University
Aalto 00076, Finland

B. Urbaszek
Department of Physics
Technische Universität Darmstadt
64289 Darmstadt, Germany
E-mail: bernhard.urbaszek@pkm.tu-darmstadt.de

A. George, A. Turchanin
Abbe Center of Photonics
07745 Jena, Germany

However, the existing synthetic routes for ML Janus TMDs, which depend on the plasma induced replacement of the top chalcogen layer of a parent TMD, are rather complex and it remains challenging to obtain large-area samples with high quality.[4,11,12] Therefore, to realize the potential of Janus TMDs for science and applications, technologically relevant methods for their fabrication still need to be established.

Here, we present a scalable and highly reproducible one-pot synthesis of high quality ML Janus SeMoS via chemical vapor deposition (CVD). It is based on a thermodynamic equilibrium approach resulting in replacement of the bottom Se layer of ML $MoSe_2$ grown on Au foil with S atoms at ≈700 °C. The Au substrate plays a crucial role in the formation of Janus SeMoS by acting as a substrate which promotes adsorption and dissociation of S clusters from the vapor phase. The formation of ML Janus SeMoS is demonstrated by angle-resolved X-ray photoelectron and Raman spectroscopy, and the growth mechanisms are confirmed by first principles calculations. Encapsulation in hBN reveals spectrally narrow excitonic emission linewidths below 20 meV at cryogenic temperatures. As a result of circularly polarized laser excitation, the free exciton peak shows strong circular polarization up to 25% that persists above liquid nitrogen temperatures while temperature dependent linewidth analysis indicates enhanced exciton–phonon coupling. In applied longitudinal magnetic fields, we obtain an exciton *g*-factor of −3.3.

2. Results and Discussion

The synthesis method of ML Janus SeMoS is schematically illustrated in **Figure 1**A. There are two-steps in our one-pot synthesis

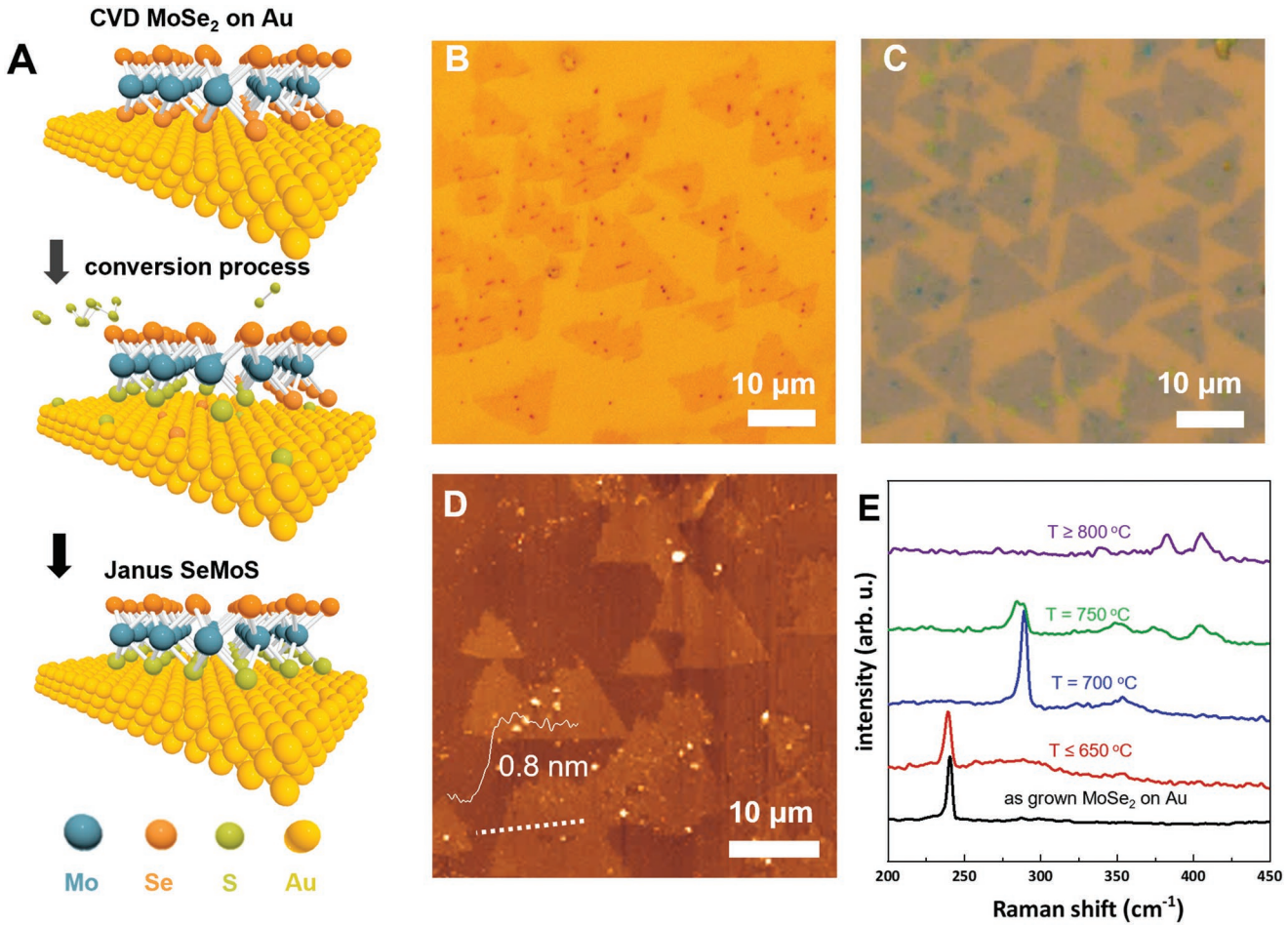

Figure 1. Synthesis and microscopic characterization of ML Janus SeMoS. A) Schematic illustration of the process for synthesizing ML Janus SeMoS. Initially, ML $MoSe_2$ is synthesized on Au foils by CVD, followed by a conversion process in which the $MoSe_2$ crystals were exposed to S vapor at 700 °C, replacing the bottom-layer Se atoms of $MoSe_2$, which is in contact with the Au surface, by S atoms to form the ML Janus SeMoS. The Au surface absorbs and catalytically dissociates the S clusters. The dissociated S atoms are mobile on the Au surface at high temperature which migrates underneath the ML $MoSe_2$ and exchanges with the Se atoms in the bottom layer. On the other hand, replacement of the top Se layer is not energetically favorable as the S clusters elastically bounced back after colliding with the top Se layer, rather than dissociating and reacting. B,C) Optical microscopy images of ML Janus SeMoS, as grown on Au foil (B) and transferred on to SiO_2/Si substrate (C). D) AFM topography image of transferred ML Janus SeMoS. The thickness of the ML Janus SeMoS is estimated as 0.8 ± 0.2 nm from the height profile shown in the inset. E) Raman spectra recorded at room temperature using 532 nm excitation wavelength on pristine ML $MoSe_2$ and ML $MoSe_2$ exposed to S vapor at different temperatures. The optimum sulfurization temperature for obtaining Janus SeMoS is 700 °C.

method. i) Our growth procedure begins with the CVD growth of ML $MoSe_2$ single crystals.[13] Subsequently, the sample is cooled down to room temperature (RT). ii) The conversion of the $MoSe_2$ into Janus SeMoS takes place upon the temperature increase and annealing at 700 °C in the presence of S vapor. The gold substrate plays an important role in the conversion, as it results in the dissociation of S molecules constituting the vapor phase[14] (S_n with n = 2, 3, 4, 6, 7, and 8) and chemisorption of the S atoms on the gold substrate.[15] Upon their diffusion underneath the $MoSe_2$ crystals, they replace the bottom Se layer thereby forming an ML Janus SeMoS. A detailed description of the experimental procedures and a schematic diagram of the CVD process is given in Figure S1 and Note S1, Supporting Information, respectively. A comparison of our synthetic approach with the previously reported methods is provided in Note S2, Supporting Information.

The above-described mechanism of ML Janus SeMoS synthesis can be understood by analyzing the energetics of the exchange processes in density-functional theory (DFT) calculations[16] (see Note S3 and Figures S2–S5, Supporting Information). We consider the adsorption and migration of S and Se atoms on the Au(111) surface as well as their interaction with the free-standing and supported $MoSe_2$ monolayer. Our calculations show that it is energetically favorable for S molecules to split upon adsorption on Au(111). The formed S adatoms are highly mobile at the temperatures used during the synthesis due to their low migration barriers (<0.4 eV). Note that it costs more than 5 eV to remove an Se atom from the top layer of the $MoSe_2$ sheet and that splitting of S molecules on this layer is energetically unfavorable. In contrast, the energy penalty for removing an Se atom from the bottom layer of the sheet followed by the immediate adsorption of this atom on the Au surface (outside the ML area) is only 1.7 eV.

In Figure 1B, an optical microscopy image of as-grown ML Janus SeMoS crystals is presented. A high density and homogeneous distribution of the triangular crystals can be clearly recognized. Figure 1C shows the Janus MLs after their transfer onto a SiO_2/Si wafer by electrochemical delamination transfer technique.[15] The atomic force microscopy (AFM) topography image of Janus SeMoS on SiO_2/Si is provided in Figure 1D. The AFM height profile (insert to Figure 1D) and the height distribution histogram (Figure S6, Supporting Information) demonstrate an average thickness of 0.8 ± 0.2 nm as expected for the ML Janus SeMoS.[4]

To better understand and optimize the conversion process, we performed a series of experiments at different sulfurization temperatures, ranging from 650 °C to 800 °C using the sulfurization time of ≈10 min. Afterward, the samples were studied by Raman spectroscopy directly on Au foils, Figure 1E. The black spectrum shows the Raman signal of as-grown ML $MoSe_2$ with the characteristic A'_1 peak at 240 cm^{-1}.[17] When the ML $MoSe_2$ is exposed to S vapor at temperatures ≤650 °C (red spectrum), the A'_1 peak is barely affected indicating there is negligible or no replacement of the Se. When the sulfurization temperature is optimized to 700 °C (blue spectrum), two characteristic Raman peaks at 290 cm^{-1} (A^1_1) and 353 cm^{-1} (E^2) are observed confirming the formation of a ML Janus SeMoS.[18] The narrow full width at half maximum (FWHM) of the A^1_1 peak (4.5 ± 0.2 cm^{-1}) indicates a high crystalline quality of the formed ML Janus SeMoS, which is consistent with our low-temperature Raman data (see below).[19] As shown in Figure S7, Supporting Information, the sulfurization at 700 °C with time <10 min resulted in the incomplete conversion (see also Note S4, Supporting Information). With further increase of temperature (green and purple spectra), significant changes in Raman spectra are observed: diminishing peak intensity, peak broadening as well as appearing of additional peaks characteristic for MoS_2. This behavior corresponds to the formation of a random $MoS_{2(1-x)}Se_{2x}$ alloy,[17,20] as expected for replacement with S of both bottom and top Se layers; for temperatures ≥800 °C, the Raman spectra are typical of highly defective ML MoS_2.[21] A comparison of the Raman spectra for as-grown Janus SeMoS MLs acquired directly on Au and after the transfer on SiO_2/Si wafers reveals identical spectroscopic characteristics showing that the transfer process can be applied in a non-invasive manner, Figure S8A, Supporting Information. A Raman map recorded on the transferred Janus ML demonstrates a uniform intensity distribution, hence proving the material homogeneity, Figure S8B,C, Supporting Information. Note that besides the individual Janus ML crystals as shown in Figure 1, also millimeter-scale homogeneous Janus ML films were synthesized by tuning the growth conditions (see Figure S9 and Note S5, Supporting Information). Our attempt to convert ML $MoSe_2$ into ML Janus SeMoS on commonly used SiO_2/Si substrate under the identical experimental conditions as used on Au foils resulted only in the formation of $MoS_{2(1-x)}Se_{2x}$ alloys (see Figure S10 and Note S6, Supporting Information). This observation further shows the crucial role of the Au surface for the successful conversion.

To further analyze the chemical composition and asymmetric structure of synthesized ML Janus SeMoS, we performed angle-resolved X-ray photoelectron spectroscopy (ARXPS)[22] of as-grown samples on Au foils, **Figure 2;** Figures S11 and S12, Supporting Information. From the binding energies (BEs) and intensities of the respective XP Mo 3d, S 2p, and Se 3d peaks, the formation of ML Janus SeMoS is clearly confirmed (see Figure 2A; Note S7 and Table S1, Supporting Information). To demonstrate the asymmetric structure of Janus SeMoS, the XP spectra were measured at various photoelectron emission angles, θ, as illustrated in the inset of Figure 2B, taking advantage of the enhanced surface sensitivity for larger θ. For each element (Se, Mo, S, and Au), the relative intensity (RI) of the XP components were calculated as a function of θ using the equation

$$\mathrm{RI} = \frac{I(x,\theta)/I\left(x,0^{\circ}\right)}{I(\mathrm{Au},\theta)/I\left(\mathrm{Au},0^{\circ}\right)} \quad (1)$$

From the variation of the RI values for Se, Mo, and S, it is seen that the Se layer is on top, followed by Mo and S at the bottom. Thus, ARXPS confirms the exchange of the bottom Se layer in ML $MoSe_2$ with S atoms, in agreement with the energetics analysis from DFT. The atomic ratio of Se:Mo:S is estimated as 0.9 ± 0.2:1.0:1.6 ± 0.2 indicating an excess amount of S atoms chemisorbed on the Au substrate. After the transfer of the ML Janus SeMoS onto an SiO_2/Si substrate, the obtained ratio is 0.8 ± 0.2:1.0:1.3 ± 0.2, which corresponds to the nearly ideal stoichiometry and suggests a loss of the excess S upon the transfer.

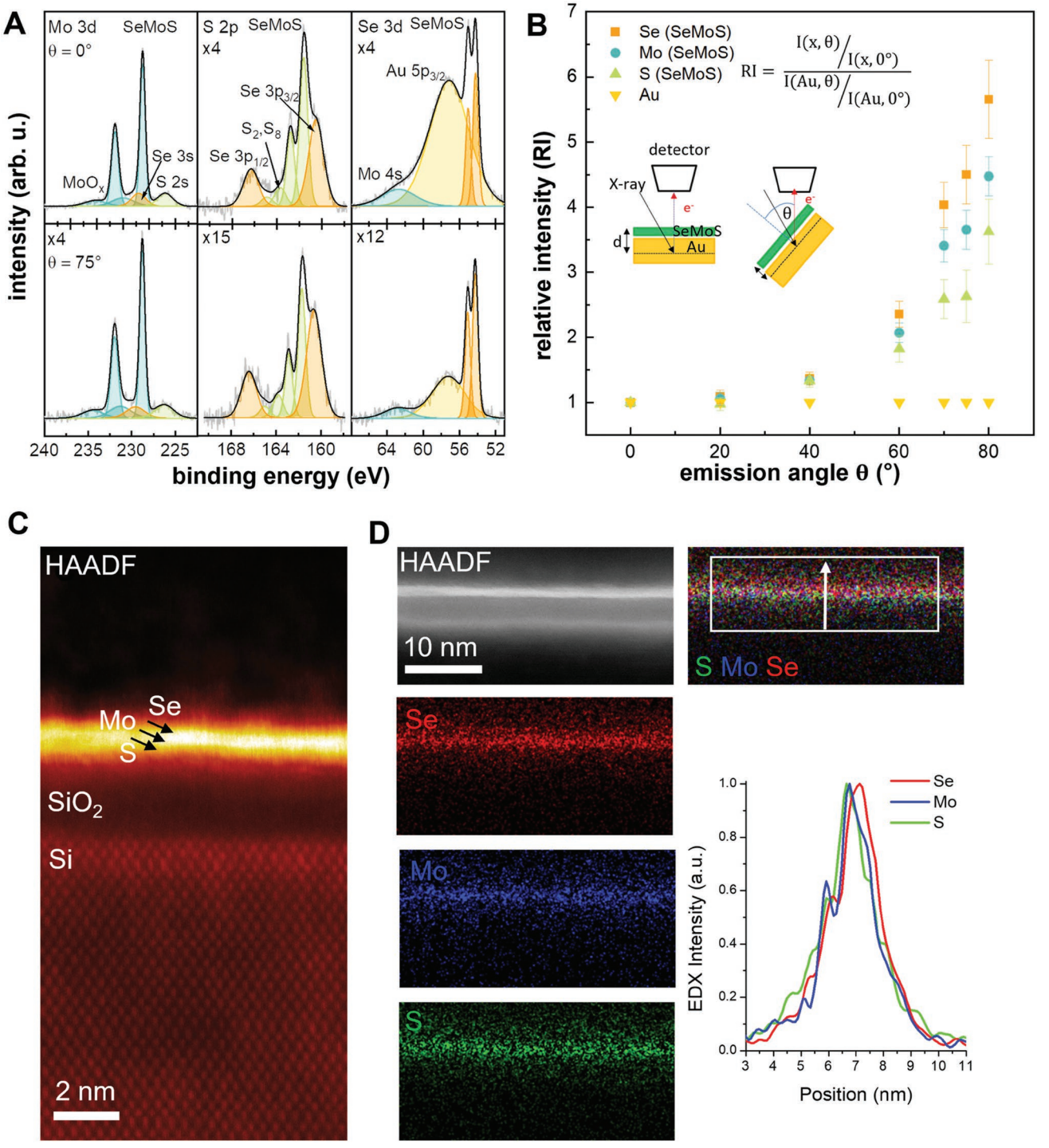

Figure 2. Angle-resolved XPS and TEM investigation of ML Janus SeMoS. A) High-resolution Mo 3d, S 2p, and Se 3d XP spectra of as-grown ML Janus SeMoS on Au foil measured at an emission angle (θ) of 0° (normal emission, top) and 75° (bottom), respectively. The fitted components have been named in the figures and discussed in detail in Note S7, Supporting Information. For better representation, the intensities of the spectra were multiplied by the factors represented in the respective figures. B) Relative intensities (RIs) of the Janus SeMoS components represented by Mo 3d, S 2p, and Se 3d peaks as well as the substrate reference Au 4f peak calculated according to the formula written in the inset are plotted for certain emission angles. Thereby, $I(x,\theta)$, $I(x,0°)$, $I(\mathrm{Au},\theta)$, and $I(\mathrm{Au},0°)$ are the intensities of each element (x = Se, Mo, S, Au) at θ and at normal emission as well as the intensities of Au at θ and at normal emission. In addition in the inset, two schemes are shown to illustrate the set-up for ARXPS ($\theta = 0°$ and 60°), whereby d is the information depth. C) Atomically resolved cross-sectional HAADF-STEM (Z-contrast) image of the interface of Janus structure on SiO_2/Si substrate. Two bright layers (Se and Mo) above a third layer (S) are visible on top of the native SiO_2 layer and the crystalline Si. The arrows mark the three different layers. D) EDX elemental maps of S, Se, and Mo together with the corresponding HAADF reference image showing three layers. The composed RGB colormap and the integrated linescan of the EDX intensity shows the ordering structure of the Janus from bottom interface to the top surface as S/Mo/Se.

Transmission electron microscopy (TEM) together with spatially resolved energy-dispersive X-ray (EDX) spectroscopy were applied to further verify the Janus SeMoS structure. The sample grown on the Au substrate was transferred to a Si wafer with a native SiO_2 layer acting as an atomically flat substrate for the cross-sectional investigation (see Figure S13, Supporting Information for the lamella preparation details). Figure 2C shows a high-angle annular dark-field (HAADF) scanning (S) TEM image of the SeMoS/SiO_2/Si interfaces. The image is dominated by *Z*-contrast where the intensity roughly scales with the power of two with heavier elements showing much brighter contrast than light elements. Two brighter layers together with the layer of lower intensity (similar contrast as the atomic columns of the Si substrate) are visible indicating the presence of two layers of heavier elements (Se and Mo) and one lighter element (S) with a similar Z-number as Si. The SeMoS structure is visible as three continuous layers instead of atomic columns corresponding to each atomic layer because there is no epitaxial relationship with the SiO_2/Si substrate. Figure S14, Supporting Information, shows an additional high resolution (HR) TEM image in the cross-sectional view. The three individual atomic layers of the Janus SeMoS structure are recognized; however, because of the different contrast mechanism of HRTEM (interference contrast); the S-, Mo-, and Se-layer appear only with very slight contrast differences. EDX elemental maps of the interface regions are shown in Figure 2D. Together with the corresponding HAADF reference map (top), three individual layers of S, Mo, and Se are clearly identified. The RGB colormap and the corresponding line profiles of the individual EDX signals show that the three layers are slightly separated from each other. The expected elemental ordering from substrate to the surface as S/Mo/Se is obtained. The local quantification of the atomic content shows a ratio of S:Mo:Se of almost 1:1:1 (Figure S15, Supporting Information). To verify also the crystalline nature of the Janus monolayer, the sample was transferred to Quantifoil TEM grids and investigated in the plane view. Figure S16, Supporting Information, shows an atomic resolved aberration corrected HRTEM image that exhibits the typical honey-comb lattice of a TMD monolayer proving the high crystallinity of the Janus SMoSe. Thus, the TEM investigation further confirms the results obtained by ARXPS and Raman spectroscopy as well as the exchange of Se atoms with S atoms at the Au interface.

Optical transition linewidths of CVD grown TMD monolayers (typically 50–100 meV) can be considerably reduced by removing the samples from the growth substrate and encapsulating them in high quality hBN.[1,23] We have applied this approach to our ML Janus SeMoS as sketched in **Figure 3**A, where the bottom (top) hBN layer is typically 50 nm (10 nm) thick. We show in Figure 3B the photoluminescence (PL) from the ML Janus SeMoS in the temperature range from 5 K to RT (see Note S1, Supporting Information for experimental details). At $T = 5$ K, the spectrum is dominated by a spectrally narrow peak (FWHM 18 meV) marked as X, visible up to RT. At low energy centered around 1.5 eV, we detect a spectrally broad transition marked L, only visible for temperatures up to 150 K.

In Figure 3C, we plot the emission energy of the X peak (exciton) as a function of temperature. Fitting the characteristic redshift of the bandgap (see Note S8, Supporting Information) allows us to extract an average phonon energy $\langle \hbar\omega \rangle$ = (38.9 ± 0.7) meV that we use in the fit of the transition linewidth as a function of temperature,[24] $\gamma = \gamma(0) + a \cdot T + \left(\beta / \left(e^{\hbar\omega/k_B T} - 1\right)\right)$, here, $\gamma(0)$ = (18.5 ± 0.1) meV is the linewidth of X at $T = 0$ K, a = (24 ± 5) μeV K^{-1} is the linear broadening due to acoustic phonons and β = (124 ± 2) meV is the strength of the phonon coupling. The value of β found here is considerably larger than the values reported previously for $MoSe_2$ and MoS_2 monolayers.[25] This value could be evidence of stronger exciton–phonon coupling for Janus layers as compared to TMD monolayers due to the intrinsic electric dipole.[26]

Janus TMD MLs are expected to possess momentum dependent spin splitting and to obey chiral optical selection rules. In Figure 3B, we detect the PL emission both co- and counter- polarized with respect to the excitation laser polarization. We extract the circular polarization degree $P_c = (I_{\sigma+} - I_{\sigma-})/(I_{\sigma+} + I_{\sigma-})$ of the X emission. For an excitation photon energy lying ≈180 meV above the X emission energy, we measure a high polarization of P_c = 25% for temperatures up to 100 K (Figure 3D) as chiral selection rules hold for the direct transition at the non-equivalent K-points at the Brillouin zone edge.[4,27] We find a drastic drop in P_c for temperatures $T > 100$ K and at 200 K we find $P_c \approx 0$. For comparison, the PL emission from localized states L is unpolarized over the investigated temperature range in Figure 3B. It is striking that for the X peak, the sudden decrease in P_c occurs over the same temperature range that sees drastic changes in the peak position and linewidth plotted in Figure 3C (see Note S8, Supporting Information, for discussion).

A key feature for ML Janus TMDs is the valley Zeeman splitting of the two exciton states in magnetic fields,[6,28] which was so far not accessible in samples with larger optical transition linewidth. In Figure 3E, we observe a clear energy difference Δ_Z between the σ^+ and the σ^- polarized PL components (see Note S8, Supporting Information) of ≈1.7 meV, at $B = 9$ T, which corresponds to an exciton Landé *g*-factor of −3.3. Interestingly, this value lies in between the Landé *g*-factor of the A-exciton in MoS_2, which is reported to be between −2 to −4, depending on background doping[6] and the A-exciton *g*-factor of $MoSe_2$ of −4.[28] In Figure 3E, the PL intensity is higher from the lower Zeeman branch, which indicates a relaxation toward the energetically lower valley branch during the exciton lifetime.

In **Figure 4**A, we show power dependent PL spectra using an HeNe laser ($\lambda = 633$ nm), and in Figure 4B, we plot the integrated PL intensity I_{PL} as a function of laser power P. The X peak intensity increases linearly with power, which is the signature of a free exciton peak, whereas for the L transition, the contributing states become saturated,[29] see Note S8, Supporting Information. In addition to our data on the energy shift and broadening with temperature, this behavior indicates that the X emission is indeed of excitonic origin. In reflectivity measurements, presented in the same panel, we distinguish the A- and B exciton resonance, marked X and X_B, respectively. The difference $\Delta_{X_B - X} \approx 177$ meV, lies between the values reported for MoS_2 and $MoSe_2$ monolayers.[30]

At the high energy part of the PL spectrum in Figure 4A close to 1.96 eV, sharp peaks corresponding to Raman scattering signals can be detected. For better visibility and comparison, we plot these spectra in Figure 4C in units of positive cm^{-1} (Stokes

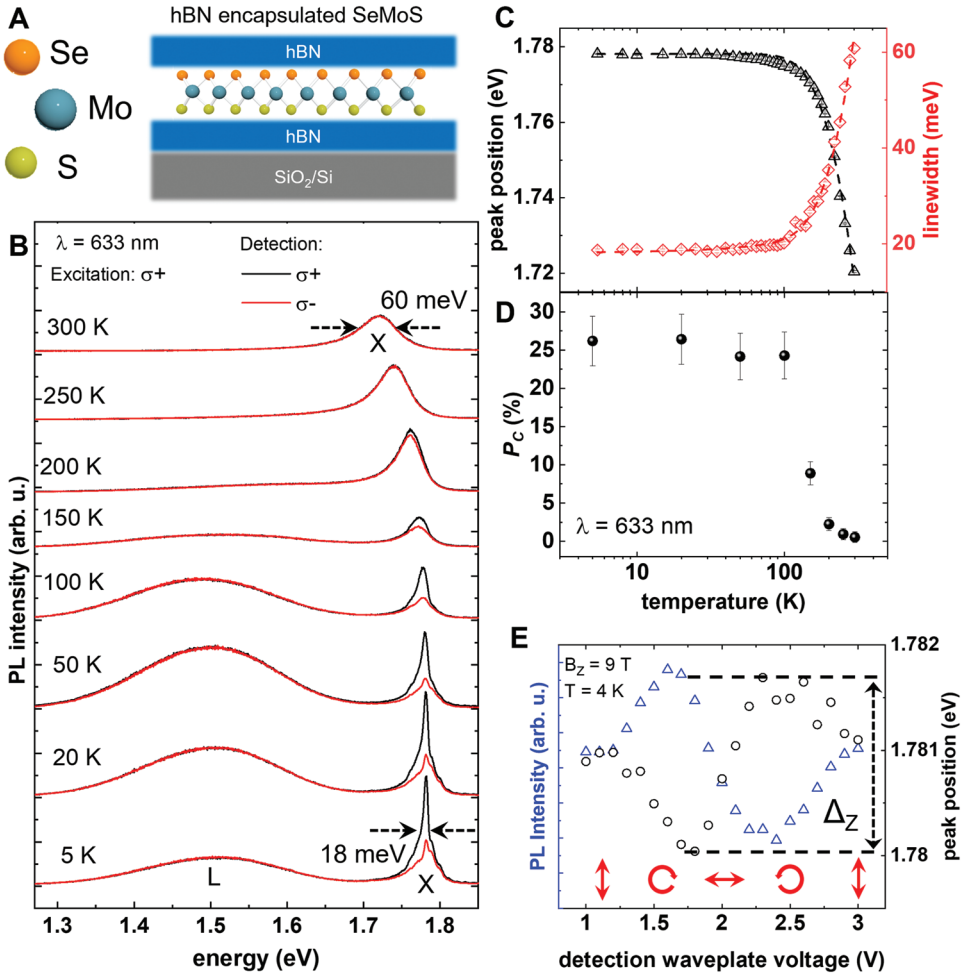

Figure 3. Temperature and valley polarization dependent optical properties of hBN-encapsulated ML SeMoS. A) Schematics of the encapsulated Janus SeMoS sample with hBN bottom and top layer. B) Temperature dependent photoluminescence (PL) spectra show the main excitonic emission (X) and up to 150 K also emission from localized states (L). For laser excitation polarization σ^+ both co-polarized (black) and counter-polarized (red) emission is plotted. C) From measurements as in (B), both the exciton transition linewidth (right axis, red symbols) and the transition energy (left axis, black symbols) are extracted and fitted, see text. D) The circular polarization degree $P_c = (I_{\sigma+} - I_{\sigma-})/(I_{\sigma+} + I_{\sigma-})$ of the PL from (A) is plotted as a function of sample temperature. The error bars correspond to the standard deviation extracted over five different areas of the sample. E) PL measurements at $T = 4$K in a magnetic field $B_z = 9$T applied perpendicular to the sample surface. The detection polarization is varied by changing the voltage applied to a liquid crystal retarder, which yields the exciton Zeeman splitting Δ_Z. Excitation with linearly polarized light (equal intensity for both circular polarization states). The red arrows indicate the detection polarization state of the liquid crystal retarder for given voltages.

shift). Our data shows the main Raman modes reported for Janus SeMoS[18] in both co- and cross-polarized detection under linear excitation and several additional, yet to be identified features. We note that the Raman peaks at ≈155 cm^{-1} and ≈175 cm^{-1}, linked to the presence of defects,[18] are comparatively weak for our samples, which is an indication of high structural quality.

We also plot in Figure 4C, the measurements in a random alloy MoSSe monolayer (hBN encapsulated) measured under the same conditions. The Raman spectra of the random alloy and the ordered Janus layer are clearly different. For the alloy, we find the MoS_2-like doublet at 400 cm^{-1} reported before in the literature.[17,20] Interestingly, the average phonon energy $\langle\hbar\omega\rangle$ = (38.9 ± 0.7) meV (corresponds to ≈313 cm^{-1}) extracted in temperature dependent measurements in Figure 3C,D, falls within the range of the main phonon energies we find in Raman spectroscopy. For further information on the electronic structure, we present in Figure 4D,E, PL measurements as a function of excitation laser energy (PLE). The data reveals a strong resonance in absorption at around 1.965 eV. By comparing with reflectivity measurements (Figure 4A), we ascribe this resonance to the B-exciton of the Janus SeMoS monolayer. Our experiments reveal that the HeNe laser excitation (633 nm; 1.96 eV) is nearly resonant with the B-exciton at $T = 4$K, which explains the comparatively high PL signal and the very rich structure in the Raman data as compared to 532 nm excitation. The PL data also shows underlying periodic features that are at a fixed energy with respect to the laser energy, likely linked to phonon assisted absorption and/or emission (Figure 4D, compare with Ref. [31]). Please note that these periodic features are absent for the random alloy monolayer sample. We plot for comparison the PLE data for the alloy monolayer, for which we find a resonance

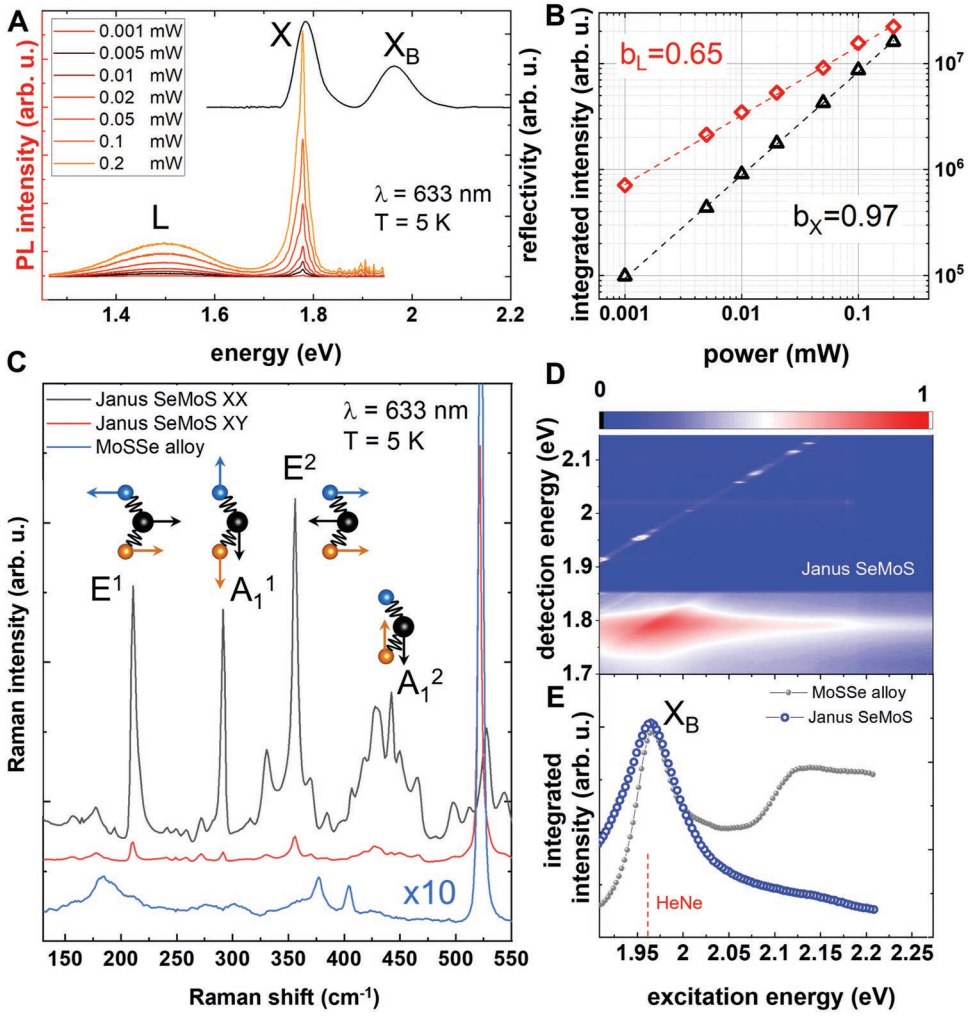

Figure 4. Photoluminescence and Raman spectroscopy of hBN encapsulated ML Janus SeMoS. A) Power dependence of PL emission at $T = 4$K. Superimposed reflectivity shows in addition the B-exciton transition (X_B). B) The slopes plotted confirm X as exciton related and L as defect related emission as we fit the data with $I_{PL}(P) = \eta P^b$. C) Comparison of Raman scattering data between SeMoS Janus monolayer (black and red graphs correspond to co- and cross-polarized detection) and MoSSe alloy monolayer (blue graph) which shows MoS_2-like doublet around 400 cm^{-1}. The main identified modes for the Janus sample are marked. D) In PL excitation spectroscopy, the laser excitation energy is varied. The X PL emission is plotted for each value of the excitation energy in a contour plot. The data also shows underlying periodic features that are at a fixed energy with respect to the laser energy, most likely linked to phonon assisted absorption and/or emission.[31] E) The same experiment as in (D) but the integrated X PL emission intensity is plotted for the Janus sample (blue circles) and the alloy monolayer (gray symbols). A strong resonance at the X_B energy is marked.

at a very similar energy position but the PLE spectrum at higher energies (>1.97 eV) is very different compared to the Janus monolayer due to the different band structure.

3. Conclusion

We have developed a simple, reproducible one-pot CVD synthesis of large-area Janus SeMoS MLs on Au foils. Their high optical quality is confirmed by a spectrally narrow excitonic emission from the Janus SeMoS MLs encapsulated in hBN. The free exciton peak shows strong circular polarization up to 25% and we extract in applied longitudinal magnetic fields an exciton valley g-factor of −3.3. Temperature dependent linewidth analysis indicates enhanced exciton–phonon coupling.

Supporting Information

Supporting Information is available from the Wiley Online Library or from the author.

Acknowledgements

The Jena group received financial support of the Deutsche Forschungsgemeinschaft (DFG) through a research infrastructure grant INST 275/257-1 FUGG (313713174), CRC 1375 NOA (Project B2, 398816777) and SPP2244 (Project TU149/13-1, 443361515). This project has also received funding from the joint European Union's Horizon 2020 and DFG research and innovation programme FLAG-ERA under grant TU149/9-1 (397373225). Ulm and Jena acknowledge financial support of the joint DFG project within grant 464283495. The authors from Toulouse received funding from the Institute for Quantum Technologies Occitanie, ANR IXTASE and the Institut Universitaire de

France. Growth of hexagonal boron nitride crystals was supported by the Elemental Strategy Initiative conducted by the MEXT, Japan, Grant Number JPMXP0112101001, JSPS KAKENHI Grant Number JP20H00354, and the CREST (JPMJCR15F3), JST. A.V.K. further thanks DFG for the support through Project KR 4866/8-1 and the Collaborative Research Center "Chemistry of Synthetic 2D Materials" SFB-1415-417590517. The authors also thank the HZDR Computing Center, HLRS, Stuttgart, Germany, and TU Dresden Cluster "Taurus" for generous grants of CPU time. The authors thank Stephanie Höppener and Ulrich S. Schubert for enabling the Raman spectroscopy and microscopy studies at the Jena Center for Soft Matter (JCSM).

Open access funding enabled and organized by Projekt DEAL.

Conflict of Interest

The authors declare no conflict of interest.

Author Contributions

Z.G., I.P., and A.E.-R. contributed equally to this work. Z.G., A.G., and A.T. designed the synthesis of Janus TMDs. A.T. directed the research. Z.G. synthesized Janus TMDs and performed basic material characterizations. E.N. and Z.G. performed the Raman spectroscopy and analysis. J.P. and C.N. performed AR-XPS and analysis. J.B., M.M, R.L, and U.K. performed the TEM investigation and analyzed the results. F.D. and A.V.K. performed the DFT calculations and contributed to the interpretation of experimental results. I.P. and A.E.R. performed encapsulation, temperature-dependent optical spectroscopy experiments, and spectral analysis. B.U., C.R., P.W., and X.M. designed the low-temperature optical spectroscopy experiments. K.W. and T.T. provided the hBN. Z.G., A.G., I.P., B.U. and A.T. wrote the manuscript with input from all co-authors.

Data Availability Statement

The data that support the findings of this study are available from the corresponding author upon reasonable request.

Keywords

2D materials, exciton–phonon coupling, high optical quality, Janus transition metal dichalcogenides, monolayers

Received: June 9, 2022
Published online: August 21, 2022

[1] I. Paradisanos, S. Shree, A. George, N. Leisgang, C. Robert, K. Watanabe, T. Taniguchi, R. J. Warburton, A. Turchanin, X. Marie, I. C. Gerber, B. Urbaszek, *Nat. Commun.* **2020**, *11*, 2391.
[2] J. Kunstmann, F. Mooshammer, P. Nagler, A. Chaves, F. Stein, N. Paradiso, G. Plechinger, C. Strunk, C. Schüller, G. Seifert, D. R. Reichman, T. Korn, *Nat. Phys.* **2018**, *14*, 801.
[3] L. M. Xie, *Nanoscale* **2015**, *7*, 18392.
[4] A.-Y. Lu, H. Zhu, J. Xiao, C.-P. Chuu, Y. Han, M.-H. Chiu, C.-C. Cheng, C.-W. Yang, K.-H. Wei, Y. Yang, Y. Wang, D. Sokaras, D. Nordlund, P. Yang, D. A. Muller, M.-Y. Chou, X. Zhang, L.-J. Li, *Nat. Nanotechnol.* **2017**, *12*, 744.
[5] J. Zhang, S. Jia, I. Kholmanov, L. Dong, D. Er, W. Chen, H. Guo, Z. Jin, V. B. Shenoy, L. Shi, J. Lou, *ACS Nano* **2017**, *11*, 8192.
[6] A. C. Riis-Jensen, T. Deilmann, T. Olsen, K. S. Thygesen, *ACS Nano* **2019**, *13*, 13354.
[7] A. Manchon, H. C. Koo, J. Nitta, S. M. Frolov, R. A. Duine, *Nat. Mater.* **2015**, *14*, 871.
[8] L. Dong, J. Lou, V. B. Shenoy, *ACS Nano* **2017**, *11*, 8242.
[9] J. Liu, S. T. Pantelides, *Phys. Rev. Lett.* **2018**, *120*, 207602.
[10] a) C. Xia, W. Xiong, J. Du, T. Wang, Y. Peng, J. Li, *Phys. Rev. B* **2018**, *98*, 165424; b) T. Zheng, Y.-C. Lin, Y. Yu, P. Valencia-Acuna, A. A. Puretzky, R. Torsi, C. Liu, I. N. Ivanov, G. Duscher, D. B. Geohegan, Z. Ni, K. Xiao, H. Zhao, *Nano Lett.* **2021**, *21*, 931.
[11] M. Yagmurcukardes, Y. Qin, S. Ozen, M. Sayyad, F. M. Peeters, S. Tongay, H. Sahin, *Appl. Phys. Rev.* **2020**, *7*, 011311.
[12] a) Y. Guo, Y. Lin, K. Xie, B. Yuan, J. Zhu, P.-C. Shen, A.-Y. Lu, C. Su, E. Shi, K. Zhang, C. HuangFu, H. Xu, Z. Cai, J.-H. Park, Q. Ji, J. Wang, X. Dai, X. Tian, S. Huang, L. Dou, L. Jiao, J. Li, Y. Yu, J.-C. Idrobo, T. Cao, T. Palacios, J. Kong, *Proc. Natl. Acad. Sci. USA* **2021**, *118*, e2106124118; b) Y.-C. Lin, C. Liu, Y. Yu, E. Zarkadoula, M. Yoon, A. A. Puretzky, L. Liang, X. Kong, Y. Gu, A. Strasser, H. M. Meyer, M. Lorenz, M. F. Chisholm, I. N. Ivanov, C. M. Rouleau, G. Duscher, K. Xiao, D. B. Geohegan, *ACS Nano* **2020**, *14*, 3896.
[13] a) A. George, C. Neumann, D. Kaiser, R. Mupparapu, T. Lehnert, U. Hübner, Z. Tang, A. Winter, U. Kaiser, I. Staude, A. Turchanin, *JPhys. Mater.* **2019**, *2*, 016001; b) E. Najafidehaghani, Z. Gan, A. George, T. Lehnert, G. Q. Ngo, C. Neumann, T. Bucher, I. Staude, D. Kaiser, T. Vogl, U. Hübner, U. Kaiser, F. Eilenberger, A. Turchanin, *Adv. Funct. Mater.* **2021**, *31*, 2101086.
[14] J. Berkowitz, J. R. Marquart, *J. Chem. Phys.* **1963**, *39*, 275.
[15] Y. Gao, Z. Liu, D.-M. Sun, L. Huang, L.-P. Ma, L.-C. Yin, T. Ma, Z. Zhang, X.-L. Ma, L.-M. Peng, H.-M. Cheng, W. Ren, *Nat. Commun.* **2015**, *6*, 8569.
[16] H.-P. Komsa, A. V. Krasheninnikov, *J. Phys. Chem. Lett.* **2012**, *3*, 3652.
[17] J. Mann, Q. Ma, P. M. Odenthal, M. Isarraraz, D. Le, E. Preciado, D. Barroso, K. Yamaguchi, G. von Son Palacio, A. Nguyen, T. Tran, M. Wurch, A. Nguyen, V. Klee, S. Bobek, D. Sun, T. F. Heinz, T. S. Rahman, R. Kawakami, L. Bartels, *Adv. Mater.* **2014**, *26*, 1399.
[18] M. M. Petrić, M. Kremser, M. Barbone, Y. Qin, Y. Sayyad, Y. Shen, S. Tongay, J. J. Finley, A. R. Botello-Méndez, K. Müller, *Phys. Rev. B* **2021**, *103*, 035414.
[19] D. B. Trivedi, G. Turgut, Y. Qin, M. Y. Sayyad, D. Hajra, M. Howell, L. Liu, S. Yang, N. H. Patoary, H. Li, M. M. Petrić, M. Meyer, M. Kremser, M. Barbone, G. Soavi, A. V. Stier, K. Müller, S. Yang, I. S. Esqueda, H. Zhuang, J. J. Finley, S. Tongay, *Adv. Mater.* **2020**, *32*, 2006320.
[20] Q. Feng, N. Mao, J. Wu, H. Xu, C. Wang, J. Zhang, L. Xie, *ACS Nano* **2015**, *9*, 7450.
[21] S. Mignuzzi, A. J. Pollard, N. Bonini, B. Brennan, I. S. Gilmore, M. A. Pimenta, D. Richards, D. Roy, *Phys. Rev. B* **2015**, *91*, 195411.
[22] R. Sant, M. Gay, A. Marty, S. Lisi, R. Harrabi, C. Vergnaud, M. T. Dau, X. Weng, J. Coraux, N. Gauthier, O. Renault, G. Renaud, M. Jamet, *npj 2D Mater. Appl.* **2020**, *4*, 41.
[23] a) S. Shree, I. Paradisanos, X. Marie, C. Robert, B. Urbaszek, *Nat. Rev. Phys.* **2021**, *3*, 39; b) A. Delhomme, G. Butseraen, B. Zheng, L. Marty, V. Bouchiat, M. R. Molas, A. Pan, K. Watanabe, T. Taniguchi, A. Ouerghi, J. Renard, C. Faugeras, *Appl. Phys. Lett.* **2019**, *114*, 232104.
[24] Y. Qin, M. Sayyad, A. R.-P. Montblanch, M. S. G. Feuer, D. Dey, M. Blei, R. Sailus, D. M. Kara, Y. Shen, S. Yang, A. S. Botana, M. Atature, S. Tongay, *Adv. Mater.* **2021**, *34*, 2106222.
[25] a) F. Cadiz, E. Courtade, C. Robert, G. Wang, Y. Shen, H. Cai, T. Taniguchi, K. Watanabe, H. Carrere, D. Lagarde, M. Manca, T. Amand, P. Renucci, S. Tongay, X. Marie, B. Urbaszek, *Phys. Rev. X* **2017**, *7*, 021026; b) M. Selig, G. Berghäuser, A. Raja, P. Nagler, C. Schüller, T. F. Heinz, T. Korn, A. Chernikov, E. Malic, A. Knorr, *Nat. Commun.* **2016**, *7*, 13279.
[26] R. Guo, X. Bu, S. Wang, G. Zhao, *New J. Phys.* **2019**, *21*, 113040.
[27] D. Xiao, G.-B. Liu, W. Feng, X. Xu, W. Yao, *Phys. Rev. Lett.* **2012**, *108*, 196802.

[28] Y. Li, J. Ludwig, T. Low, A. Chernikov, X. Cui, G. Arefe, Y. D. Kim, A. M. van der Zande, A. Rigosi, H. M. Hill, S. H. Kim, J. Hone, Z. Li, D. Smirnov, T. F. Heinz, *Rev. Lett.* **2014**, *113*, 266804.
[29] I. Pelant, J. Valenta, *Luminescence Spectroscopy of Semiconductors*, Oxford University Press, Oxford, UK **2012**.
[30] A. Kormányos, G. Burkard, M. Gmitra, J. Fabian, V. Zólyomi, N. D. Drummond, V. Fal'ko, *2D Mater.* **2015**, *2*, 022001.
[31] I. Paradisanos, G. Wang, E. M. Alexeev, A. R. Cadore, X. Marie, A. C. Ferrari, M. M. Glazov, B. Urbaszek, *Nat. Commun.* **2021**, *12*, 538.